

Numerical Study of Compressible Magnetohydrodynamic Turbulence in Two Dimensions

Hyesook Lee¹, Dongsu Ryu¹, Jongsoo Kim², T. W. Jones³, and Dinshaw Balsara⁴

ABSTRACT

We have studied forced turbulence of compressible magnetohydrodynamic (MHD) flows through two-dimensional simulations with different numerical resolutions. First, hydrodynamic turbulence with Mach number $\langle M_s \rangle_{\text{init}} \equiv \langle v \rangle_{\text{rms}}/c_s = 1$ and density compression $\langle \delta\rho/\rho \rangle_{\text{rms}} \simeq 0.45$ was generated by enforcing a random force. Then, initial, uniform magnetic fields of various strengths were added with Alfvénic Mach number $\langle M_A \rangle_{\text{init}} \equiv \langle v \rangle_{\text{rms}}/c_{A,\text{init}} \gg 1$. An isothermal equation of state was employed, and no explicit dissipation was included. In our simulations, the maximum amplification factor of magnetic energy depends on resolution and is proportional to $n_x^{1.32}$, where n_x is the number of grid cells spanned by the computational box size. After the MHD turbulence is saturated, the resulting flows are categorized as very weak field (VWF), weak field (WF), and strong field (SF) classes, which have $\langle M_A \rangle \equiv \langle v \rangle_{\text{rms}}/\langle c_A \rangle_{\text{rms}} \gg 1$, $\langle M_A \rangle > 1$, and $\langle M_A \rangle \sim 1$, respectively. The flow character in the VWF cases is similar to that of hydrodynamic turbulence. In the WF cases, magnetic energy is still smaller than kinetic energy in the global sense, but magnetic field can become locally important. Hence, not only in the SF regime but also in the WF regime, turbulent transport is suppressed by the magnetic field. In the SF cases, the energy power spectra in the inertial range, although no longer power-law, exhibit a range with slopes close to ~ 1.5 , hinting the Iroshnikov-Kraichnan spectrum. These characteristics of the VWF, WF, and SF classes are consistent with their incompressible turbulence counterparts, indicating that a modest compressibility of $\langle \delta\rho/\rho \rangle_{\text{rms}} \lesssim 0.45$, or so, does not play a significant role in turbulence. Our simulations were able to produce the SF class behaviors only with high resolution

¹Department of Astronomy & Space Science, Chungnam National University, Daejeon 305-764, Korea: lhs@canopus.chungnam.ac.kr, ryu@canopus.chungnam.ac.kr

²Korea Astronomy Observatory, 61-1, Hwaam-Dong, Yusong-Ku, Taejon 305-348, Korea: jskim@kao.re.kr

³Department of Astronomy, University of Minnesota, Minneapolis, MN 55455: twj@msi.umn.edu

⁴Department of Physics, University of Notre Dame, Notre Dame, IN 46556: dbalsara@nd.edu

of at least 1024^2 grid cells. With lower resolutions, we observed the formation of a dominant flux tube, which accompanies the separation of magnetic field from the background flow. The specific requirements for the simulation of the SF class should depend on the code (and the numerical scheme) as well as the initial setup, but our results do indicate that very high resolution would be required for converged results in simulation studies of MHD turbulence.

Subject headings: methods: numerical –MHD – turbulence

1. Introduction

The existence of cosmic magnetic fields in diffuse astrophysical plasmas (the interstellar media in galaxies, the intracluster media in clusters of galaxies and even the media associated with filaments and superclusters of galaxies) have been recognized for a while (for reviews, see *e.g.*, Kronberg 1994; Beck *et al.* 1996; Zweibel & Heiles 1997; Carilli & Taylor 2002; also see Ryu *et al.* 1998; Clarke *et al.* 2001). Although the origin of such fields is not yet fully understood, turbulence is known to play an important role in the amplification and diffusion of existing magnetic fields. For instance, magnetic fields grow effectively by turbulent motion of conducting fluids (the α effect), but they are not further amplified when Maxwell stresses become strong enough to affect the turbulent motion itself. How strong the magnetic fields would be in order to influence turbulence is one of the intriguing topics in magnetohydrodynamic (MHD) turbulence. It has been argued through two-dimensional incompressible simulations that turbulent transport is reduced by weak magnetic fields whose energy is small compared to the kinetic energy of turbulent flows (Cattaneo & Vainshtein 1991; Cattaneo 1994). A similar suppression was also observed in three-dimensional simulations of incompressible flows (Tao *et al.* 1993). It is an important issue in astrophysics, since it is a part of the process for the generation and evolution of cosmic magnetic fields (see *e.g.*, Ruzmaikin *et al.* 1988; Kulsrud *et al.* 1997; Kulsrud 1999).

In this work, we study compressible MHD turbulence by solving the ideal MHD equations with an isothermal equation of state. Since turbulent motion produces structures spanning a wide range of scales with accompanying energy transfer among different scales, high spatial resolution is required to cover a sufficient inertial range. Hence, in this paper we present high resolution two-dimensional simulations using up to 1536^2 grid cells, leaving three-dimensional simulations for follow-up work. In addition, in order to achieve the highest possible magnetic Reynolds number and Reynolds number, no dissipation was included explicitly in our simulations. However, the resistivity and viscosity of numerical origin are still effective as small-scale dissipative channels. From the simulations, we examine the ba-

sic properties of the resulting MHD turbulence. We also address the dependence of the properties on resolution, including the amplification of magnetic field.

The rest of the paper is organized as follows. In the next section, we describe the problem setup as well as the code properties. In §3 and §4, we present the results of simulations of hydrodynamic and MHD turbulence. Finally in §5, the findings of this study are summarized.

2. Numerics

In simulations of compressible MHD turbulence, gas is heated by shocks and reconnection events, as well as numerical dissipation that mimics viscous and resistive influences (see below). Hence, in order to maintain the turbulence statistically in a steady-state, cooling should be applied to the internal energy. One simple way to handle it is to assume the isothermality of flows. The MHD equations of compressible, isothermal gas are

$$\frac{\partial \rho}{\partial t} + \vec{\nabla} \cdot (\rho \vec{v}) = 0, \quad (1)$$

$$\frac{\partial \vec{v}}{\partial t} + \vec{v} \cdot \vec{\nabla} \vec{v} + \frac{c_s^2}{\rho} \vec{\nabla} \rho - \frac{1}{\rho} (\vec{\nabla} \times \vec{B}) \times \vec{B} = \vec{f}, \quad (2)$$

$$\frac{\partial \vec{B}}{\partial t} - \vec{\nabla} \times (\vec{v} \times \vec{B}) = 0, \quad (3)$$

with an additional constraint

$$\vec{\nabla} \cdot \vec{B} = 0, \quad (4)$$

for the absence of magnetic monopoles. Here, c_s is the isothermal sound speed, and the units are chosen so that the factor of 4π does not appear in the equations. To enforce turbulence, a random force per mass, $\vec{f} = f_x \hat{x} + f_y \hat{y}$, was added. It has the following form:

$$f_{x,y}(x, y, t) = v_{\text{amp}} \cos(\omega t + \delta_t) \cos(k_{in,x} x + \delta_x) \cos(k_{in,y} y + \delta_y), \quad (5)$$

where δ_t , δ_x , and δ_y are random phases in the range of $0 \leq \delta_t, \delta_x, \delta_y \leq \pi$.

The above equations were solved using a multi-dimensional MHD code described in Kim *et al.* (1999), which is specifically designed for isothermal MHD. It is based on the explicit, finite-difference Total Variation Diminishing (TVD) scheme, which is a second-order accurate upwind scheme, and employs the minmod flux limiter. Simulations were performed in the computational domain of $x = [0, L]$, $y = [0, L]$, and $L = 1$ with a periodic boundary condition using $n_x^2 = 256^2, 512^2, 1024^2$ and 1536^2 grid cells. The total mass in the computational box is conserved, and the averaged density was set to be $\langle \rho \rangle = \rho_0 = 1$. The

values of other parameters in the simulations are the following: the isothermal sound speed $c_s = 1$, the angular frequency of the random forcing $\omega = 2\pi$, and the input wavenumbers $k_{in,x,y} = 8\pi$. With this choice, we note that the input scale of the random forcing is one quarter of the computational box size and the period is one sound wave crossing time across the box. The amplitude of the random forcing, v_{amp} , was set so that without a magnetic field, hydrodynamic turbulence is saturated with the averaged Mach number $\langle M_s \rangle_{\text{init}} \equiv \langle v \rangle_{\text{rms}}/c_s = 1$ (see §3). MHD turbulence was generated by introducing uniform magnetic fields of various strength into the saturated hydrodynamic turbulence (see §4).

Although our simulations do not contain explicit resistivity or viscosity, unavoidable numerical diffusion of magnetic field and momentum across cell produce effective numerical resistivity and viscosity, respectively. Kim *et al.* (1999) studied the character of numerical dissipation in the code used for this work through the decay of a two-dimensional Alfvén wave. They showed that for waves spanning different numbers of grid cells, n , the effective magnetic Reynolds number and Reynolds number are proportional to $n^{1.66}$, mimicking the “hyper-type” resistivity and viscosity ($\eta \nabla^4 \vec{B}$ and $\mu \nabla^4 \vec{v}$) rather than the “normal-type” resistivity and viscosity ($\eta \nabla^2 \vec{B}$ and $\mu \nabla^2 \vec{v}$) that characterize the physical dissipation of “collisional” fluids. They also estimated that the effective Reynolds numbers are larger than several hundreds if $n \geq 8$, so that the inertial range covers scales spanning 8 grid cells or more. We note that numerical dissipation estimates depend somewhat on the tests used. For instance, the test suggested by Zweibel *et al.* (2002) would have given somewhat smaller numerical dissipation. Hence, our estimation of the inertial range based on the Alfvén wave decay can be regarded to be rather conservative.

In most numerical studies of astrophysical turbulence based on explicit dissipation, the normal-type resistivity and viscosity have been included explicitly. However, dissipation processes in diffuse astrophysical plasmas are not well understood, and it is unlikely that the dissipation can be modeled by way of simple resistivity and viscosity coefficients. Hence, more careful consideration would be required in the studies of the properties of astrophysical turbulence when details on dissipative scales become important. In this paper we are concerned mostly with the properties of turbulence in the inertial range, which would be less sensitive to the form of dissipation, so we ignore dissipative complications outside this range.

3. Hydrodynamic Turbulence

Simulations of hydrodynamic turbulence were first performed for two reasons. One is to generate the initial states for MHD simulations. The other is to observe the change of

turbulence properties from the hydrodynamic case under the influence of magnetic fields. In the absence of magnetic fields, a trans-sonic turbulence with $\langle M_s \rangle_{\text{init}} \simeq 1$ developed (see Table 2).

Figure 1 shows a typical resulting density distribution at an epoch $t = 15$ and the time-averaged power spectrum of kinetic energy in the simulation with 1536^2 grid cells. The existence of weak shocks is evident in the density image. Here, “weak” means the shock Mach number is small; typically $M_{\text{shock}} \sim 2$. The density compression is $\langle \delta\rho/\rho \rangle_{\text{rms}} \simeq 0.45$, when averaged over space and time in all the simulations of all resolutions (see Table 3). In a two-dimensional system, the forced turbulence of “incompressible” flows exhibits the dual energy spectrum known as the Kraichnan spectrum: in the range of $k < k_{\text{in}}$, the slope follows $k^{-5/3}$ indicating the direct cascade of energy, while in the range of $k > k_{\text{in}}$, it follows k^{-3} meaning the direct cascade of enstrophy (see *e.g.*, Lesieur 1997 and references therein). In the case of “high compressibility,” where strong shocks are common, the energy spectrum follows the k^{-2} slope in the inertial range, known as the Burgers spectrum (see *e.g.*, Lesieur 1997 and references therein). In our results with weak compressibility, the energy spectrum is consistent with the Kraichnan spectrum as shown in the right panel of Figure 1, but the slope for $k > k_{\text{in}}$ is ~ 2.72 ; somewhat shallower than for incompressible turbulence. As listed in Table 4, the deviation of the slope from k^{-3} increases systematically as the resolution increases. This is because in higher resolution simulations, shocks are better resolved, and, hence, their effect is more evident in the energy power spectrum.

4. MHD Turbulence

Weak, uniform magnetic fields of various strength were added to the fully developed hydrodynamic turbulence. In the $n_x^2 = 256^2, 512^2$ and 1024^2 simulations, the flows of hydrodynamic turbulence at $t = 30$ were taken as the initial states, while in the 1536^3 simulations, the flow at $t = 15$ (the right panel of Figure 1) was taken. The strength of the added magnetic fields was set so that the initial Alfvénic Mach number, $\langle M_A \rangle_{\text{init}} \equiv \langle v \rangle_{\text{rms}}/c_{A,\text{init}}$, ranged from 1000 to 10 (it corresponds to the plasma β of 2×10^6 to 200). The Alfvénic Mach number represents the ratio of Reynolds stresses to Maxwell stresses, so is a convenient way to characterize magnetic field strength in these flows.

The magnetic field strength grew rapidly, almost exponentially, during the initial transient period, and then saturated. Figure 2 shows the time evolution of rms magnetic field strength and flow velocity. The resulting flows of MHD turbulence after saturation can be naturally categorized into *very weak field* (VWF), *weak field* (WF) and *strong field* (SF) classes (Table 1). In the VWF cases, magnetic field influences are negligible, and the flow

velocity does not change noticeably from purely hydrodynamic turbulence. In the WF cases, the magnetic field energy, E_{mag} , is still small compared to the flow kinetic energy, E_{kin} , but the magnetic field does locally affect small scale flow motions. Hence, the turbulence flow velocity is decreased from that of non-magnetic cases. Finally, the cases where E_{mag} becomes comparable to E_{kin} are classified as the SF class. We note that the change in the flow properties is gradual with the increase of the strength of the initial, uniform fields. Hence, boundaries between the classes are somewhat arbitrary. We set the criterion for the boundary between the VWF and WF classes as $\langle M_s \rangle \equiv \langle v \rangle_{rms}/c_s \lesssim 1$; more specifically, $\langle M_s \rangle = 0.9$ was taken. On the other hand, the criterion for the boundary between the WF and SF classes was set as $\langle M_A \rangle \equiv \langle v \rangle_{rms}/\langle c_A \rangle_{rms} \gtrsim 1$, more specifically $\langle M_A \rangle = 2$ was taken. Among the SF cases, we observed examples where there a change in the magnetic field configuration takes place. In particular there are cases in which a dominant flux tube develops. These cases we categorized specifically as the *field separation* (FS) class. The growth of magnetic field strength and the characteristics of the four classes are further detailed in the following subsections.

For quantitative discussions we computed, in addition to $\langle M_A \rangle$ and $\langle M_s \rangle$ (Table 2), the density compression, $\langle \delta\rho/\rho \rangle_{rms}$, and the intermittency (or the kurtosis of the field distribution) $I \equiv \langle B^4 \rangle_{rms}/\langle B^2 \rangle_{rms}^2$ (Table 3), as well as the slopes of the power spectra of kinetic and total energies (Table 4). Note that with a Gaussian distribution of magnetic field, $\vec{B} \propto \exp(-x^2/2\sigma^2)\hat{y}$, the value of I is 2.39 when summed over the interval $-3\sigma \leq x \leq 3\sigma$, or 3.99 when $-5\sigma \leq x \leq 5\sigma$ is taken into account.

4.1. Growth of Magnetic Field Strength

There is no dynamo action in two-dimensions, and the total magnetic flux through given boundaries is conserved. Hence, the growth of magnetic field strength shown in Figure 2 is due to stretching and compression. The growth stops either when the magnetic energy reaches an equipartition with the kinetic energy, so that the back-reaction from magnetic field Maxwell stresses plays a dominant role, or when the separation between magnetic sheets is reduced to the diffusive scale, so that reconnection takes place (see *e.g.*, Biskamp 1993 for details). If the initial, uniform magnetic field is weak enough, the growth is saturated by the latter cause before the magnetic energy reaches equipartition, as in the VWF and WF cases. Then, the resulting growth should depend on the diffusive scale and, hence, on the effective resistivity. Then the amplification of magnetic energy from the initial value is expected to be $\lesssim (k_{in}\delta)^{-2} \sim R_m$ (see *e.g.*, Biskamp 1993). Here, δ is the diffusive scale and R_m is the magnetic Reynolds number.

Figure 3 shows the averaged amplification of magnetic energy in our simulations as a function of grid resolution. Only the VWF and WF cases were considered, because in the SF cases, the growth of magnetic field stopped as a consequence of Maxwell stresses, rather than reconnection. The amplification shown in the figure is proportional to $n_x^{1.32}$. Furthermore, with $R_m \propto n^{1.66}$ for our code (see §2), the amplification is estimated to be approximately proportional to $R_m^{0.8}$, which is somewhat shallower than the expected dependence ($\propto R_m$). However, this result agrees well with results of two-dimensional numerical simulations for incompressible MHD turbulence (Biskamp 1993).

4.2. VWF Cases

The VWF class includes those cases where the back-reaction of magnetic field into flow motions is insignificant. The criterion $\langle M_s \rangle \gtrsim 0.9$ corresponds to the rms velocity decrease by less than 10%. The characteristics of turbulence in these cases are summarized as follows: 1) The density compression is still large with $\langle \delta\rho/\rho \rangle_{\text{rms}} \gtrsim 0.38$ (Table 3) and shocks still exist as shown clearly in the bottom-left panel of Figure 4. 2) The intermittency is large with $I \gtrsim 3.5$ (Table 3), which indicates that the spatial contrast in the magnetic field strength distribution is high. In particular, the bottom-right panel of Figure 4 shows that the magnetic field is mostly thin tubes (or thin sheets in extension to the third dimension). 3) The Alfvén Mach number is $\langle M_A \rangle \lesssim 4.5$ (Table 2), and hence the kinetic energy is, at least, an order of magnitude larger than the magnetic energy. Also, the power of kinetic energy, P_k^{kin} , is larger than that of magnetic energy, P_k^{mag} , over most wavenumbers, as shown in the bottom panels of Figure 5. However, $P_k^{\text{mag}} \gtrsim P_k^{\text{kin}}$ in a small range of large wavenumbers. This is because the magnetic field first built up on small scales. However, it saturated due to reconnection before the power could extend to larger scales. 4) The slope of P_k^{kin} was not affected much by the magnetic field. The change was less than a few percent as shown in Table 4. But the slope of the power of the total energy, P_k^{tot} , changed significantly compared to the hydrodynamic case, especially in the MHD cases close to the boundary between the VWF and WF classes. This is because the small scale power of magnetic energy pushed P_k^{tot} up, and hence P_k^{tot} does not have a single, well-defined slope any more.

4.3. WF Cases

The WF class was categorized by the property that globally the magnetic energy is smaller than the kinetic energy, but yet the back-reaction of magnetic field is not negligible. As the criterion to represent this property, $\langle M_s \rangle \lesssim 0.9$ and $\langle M_A \rangle \gtrsim 2$ were adopted (Table 2).

The characteristics of turbulence in these cases are the following: 1) As shown in the middle-left panel of Figure 4, the occurrence of shocks is reduced and their strength is weakened compared to the hydrodynamic case. The density compression is $0.28 \lesssim \langle \delta\rho/\rho \rangle_{\text{rms}} \lesssim 0.38$ (Table 3), which is smaller than that in the VWF cases. 2) The contours of magnetic field lines plotted in the middle-right panel of Figure 4 show the appearance of almost circular magnetic islands. At the same time, the magnetic field is less concentrated than in the VWF cases, with smaller intermittency $2.2 \lesssim I \lesssim 3.5$ (Table 3). 3) Although in the small wavenumber region the magnetic energy power is still smaller than the kinetic energy power, $P_k^{\text{mag}} \ll P_k^{\text{kin}}$, at large wavenumbers, $P_k^{\text{mag}} \gtrsim P_k^{\text{kin}}$, as shown in the middle panels of Figure 5. Hence, turbulent transport can be suppressed by magnetic fields on the small scales where $P_k^{\text{mag}} \gtrsim P_k^{\text{kin}}$. Consequently, the flow velocity decreases noticeably from that of hydrodynamic turbulence (see Figure 2). 4) The power of magnetic energy, P_k^{mag} , changed the shape of P_k^{tot} as well as that of P_k^{kin} in power spectra, and the slopes are not simply defined over the entire inertial range of wavenumber any more (see Figure 5). We calculated the slopes of P_k^{kin} and P_k^{tot} over $2 \times k_{\text{in}} \leq k \leq k_{24}$, where the slopes are relatively well defined, and listed them in Table 4. Here, k_{24} is the wavenumber corresponding to 24 grid cells. The slope of P_k^{kin} is significantly smaller than those of the hydrodynamic and VWF cases. The slope of P_k^{tot} is quite small. But this is because P_k^{mag} peaks in the wavenumber range over which the slope was calculated (see Figure 5).

4.4. SF Cases

In the SF cases, the magnetic energy grows to become comparable to the kinetic energy, with $\langle M_A \rangle \lesssim 2$ at saturation (Table 2). Hence, the flow velocity is influenced significantly by magnetic field (Figure 2), with $\langle M_s \rangle \lesssim 0.75$ at saturation (Table 2). The characteristics of SF turbulence are the following: 1) With the significantly reduced Mach number, shocks are rare, as shown in the top-left panel of Figure 4. The density compression is accordingly reduced to $\langle \delta\rho/\rho \rangle_{\text{rms}} \lesssim 0.28$ (Table 3). 2) As shown in the top-right panel of Figure 4, circular magnetic flux islands, or loops, are common. This trend of changing topology in magnetic field lines, from tubes to loops, with increase of magnetic field strength was observed also in the two-dimensional simulations of incompressible MHD turbulence (see *e.g.*, Biskamp 1993). At the same time, the spatial contrast of magnetic field strength distribution becomes low with smaller intermittency $I \lesssim 2.2$ (Table 3). 3) The power of magnetic energy exceeds that of kinetic energy with $P_k^{\text{mag}} \gtrsim P_k^{\text{kin}}$ over all $k \gtrsim k_{\text{in}}$ as shown in the top panels of Figure 5, although still $P_k^{\text{mag}} < P_k^{\text{kin}}$ in $k \lesssim k_{\text{in}}$. 4) The slopes of P_k^{kin} and P_k^{tot} , calculated over $2 \times k_{\text{in}} \leq k \leq k_{24}$ as in the WF cases, are listed in Table 4. Across the above wavenumber range, P_k^{kin} , P_k^{tot} and P_k^{mag} all exhibit a single slope close to ~ 1.5 ; namely, the slope of

the Iroshnikov-Kraichnan spectrum (the top panels of Figure 5).

We note that the emergence of the slope of ~ 1.5 is achieved only in the very high resolution simulations with 1024^2 and 1536^2 grid cells, not in the simulations with 256^2 and 512^2 grid cells. In fact, there is no case categorized as the SF class in the simulations with 256^2 and 512^2 grid cells at all (see Table 1). That is, our two-dimensional simulations of MHD turbulence start to show converged behaviors with 1024^2 grid cells or more.

4.5. FS Cases

The cases with $\langle M_A \rangle_{\text{init}} \lesssim 30$ show FS class behavior, wherein a dominant flux tube forms, and, as a consequence, the magnetic field separates from the background flow (see Fig. 6). In such FS cases, flows become anisotropic and their characteristics are different from the other cases. The appearance of this behavior can be understood as follows. Recall that there are three ideal 2D MHD invariants; the total energy, E_{tot} , the mean square of the magnetic potential, A , and the cross helicity,

$$K = \frac{1}{2} \int \vec{v} \cdot \vec{B} d^2 \vec{x}. \quad (6)$$

Among them, the power spectrum of A exhibits an inverse cascade, while the power spectra of E_{tot} and K exhibit a normal cascade (see *e.g.*, Biskamp 1993). Hence, just as in three dimensions, large scale magnetic field power can be built up in the regime $k \leq k_{\text{in}}$ in two-dimensional MHD turbulence. In our FS cases this power build-up proceeds through the formation of a magnetic flux tube with a coherent length larger than the scale associated with k_{in} . However, as pointed out in §4.1, there is no dynamo action in our simulations. Hence, the formation of such a flux tube should involve reconnection followed by the expulsion of gas out of the flux tube, reducing the gas density (so, also the gas pressure) inside the tube, while maintaining approximate pressure equilibrium.

We note that the critical value of $\langle M_A \rangle_{\text{init}}$ for the FS class is independent of numerical resolution in our simulations (see Table 1). This is because the existence of the flux tube depends on its ability to resist ram pressure bending, which depends on large scale flows, so is independent of numerical resolution. On the other hand, since the formation of the dominant flux tube involves reconnection, we expect the time to reach the state where the magnetic field separates from the background flow would depend on resistivity. The flux tube was developed in a few tens eddy turnover times in our simulations. However, in astrophysical environments such as interstellar media or intracluster media, the resistivity is much smaller than that of our simulations. The classical magnetic Reynolds number in the interstellar medium can be as large as 10^{50} or so (see *e.g.*, Spitzer 1979). Hence, we expect that the

emergence of the flux tube would take too long in astrophysical environments, and instead, turbulence of the SF class is more likely to develop. So the failure of SF cases in our 256^2 and 512^2 simulations is probably a limitation of numerical simulations; in particular from very large numerical resistivity compared to astrophysical environments and perhaps also from the periodic boundary we employed.

5. Summary & Conclusion

We performed high resolution two-dimensional simulations of isothermal MHD turbulence using up to 1536^2 grid cells. Compressibility was taken into account, with Mach numbers $\langle M_s \rangle \lesssim 1$. In order to maximize the magnetic Reynolds number and the Reynolds number, no explicit dissipation was included. Instead, resistivity and viscosity of numerical origin were utilized. Our findings are summarized as follows:

- 1) The growth of magnetic energy from the initial value depends on effective resistivity and, hence, on resolution. We measured a maximum magnetic energy amplification proportional to $n_x^{1.32}$. After the growth saturated, the turbulence could be categorized into three classes, which we labeled very weak field (VWF), weak field (WF), and strong field (SF) classes, depending on the strength of the uniform component of magnetic fields, or equivalently the initial Alfvén Mach number, $\langle M_A \rangle_{\text{init}}$. Each class is characterized by different turbulence properties.
- 2) In the WF cases, although $E_{\text{mag}} < E_{\text{kin}}$ globally, the rms flow velocity decreases due to the magnetic field, which can become locally important. That is, even a weak magnetic field reduces turbulent transport (Cattaneo & Vainshtein 1991; Cattaneo 1994).
- 3) Although the inertial range power spectra of MHD turbulence are not represented by power-laws any more, part of the inertial range still develops a slope close to ~ 1.5 ; that of the Iroshnikov-Kraichnan spectrum, in the SF cases. Such a slope developed only in highest resolution simulations with 1024^2 and 1536^2 grid cells.
- 4) In the lower resolution simulations with 256^2 and 512^2 grid cells, there are no cases categorized as the SF class. Instead, with $\langle M_A \rangle_{\text{init}} \lesssim 30$, those simulations developed into FS cases, where a large flux tube dominates the flow structures and separates the flow from the magnetic field. This FS property is the result of large numerical resistivity along with the periodic box used.

The conclusions of our work are the following:

- 1) For the VWF, WF, and SF cases, we observed properties of turbulence which are consistent with those of incompressible counterparts, whenever comparisons are made. Hence, we conclude that weak compressibility of $\langle \delta\rho/\rho \rangle_{\text{rms}}$ up to ~ 0.45 would not be important in

characterizing MHD turbulence.

2) Converged behavior in simulated turbulence, such as that of the SF class, starts to appear only in simulations with very high resolution, 1024^2 grid cells or more, in our simulations. The fact that simulations with 1024^2 grid cells or more are necessary for our two-dimensional study of MHD turbulence points to the need of very high resolution in three-dimensional MHD turbulence studies as well. For hydrodynamic turbulence, Porter *et al.* reported that converged results emerged with 512^3 or more grid cells in their simulations. However, we note that numerical dissipation would differ in different codes based on different schemes. As a result, the convergence behavior would be different, too. These findings emphasize the importance in turbulence studies of high resolution grids and codes with the smallest possible numerical dissipation. Any explicit treatment of dissipation will require even higher resolution simulations, since numerical dissipation and diffusion would have to be smaller than the explicit terms.

The work by HL and DR was supported by an international collaboration grant from Korea (KOSEF F01-2000-000-10009-0) and Germany (DFG). The work by JK was supported by Strategic National R&D Program (M10222000005-02B0600-00400) from MOST, Korea. The work by TWJ was supported by the National Science Foundation (AST96-19438; AST00-71167) and the University of Minnesota Supercomputing Institute. Simulations were made through the support by “The Supercomputing Application Support Program of KISTI”.

REFERENCES

- Beck, R., Brandenburg, A., Moss, D., Shukurov, A. & Sokoloff, D. 1996, ARA&A, 34, 155
- Biskamp, D. 1993, Nonlinear Magnetohydrodynamics (Cambridge: Cambridge Univ. Press)
- Carilli, C. L. & Taylor, G. B. 2002, ARA&A, 40, in press (astro-ph/0110655)
- Cattaneo, F. 1994, ApJ, 434, 200
- Cattaneo, F. & Vainshtein, S. I. 1991, ApJ, 376, L21
- Clarke, T. E., Kronberg, P. P. & Böhringer, H. 2001, ApJ, 547, L111
- Kim, J., Ryu, D., Jones, T. W. & Hong, S. 1999, ApJ, 514, 506
- Kronberg, P. P. 1994, Rep. Prog. Phys. 57, 325
- Kulsrud, R. M. 1999, ARA&A, 37, 37

- Kulsrud, R. M., Cen, R., Ostriker, J. P. & Ryu, D. 1997, *ApJ*, 480, 481
- Lesieur, M. 1997, *Turbulence in Fluids*, 3rd ed. (Dordrecht: Kluwer)
- Porter, D., Pouquet, A. & Woodward, P. 1998, *Phys. Fluid*, 10, 237
- Ryu, D., Kang, H., & Biermann, P. L. 1998, *A&A*, 335, 19
- Ruzmaikin, A.A., Shukurov, A.M. & Sokoloff, D.D. 1988, in *Astrophysics and Apace Science Library, Magnetic Fields in Galaxies*, (Dordrecht: Kluwer)
- Spitzer, L. 1979, *Physical Processes in the Interstellar Medium* (New York: Wiley-Interscience)
- Tao, L., Cattaneo, F. & Vainshtein, S. I. 1993, in *Theory of Solar and Planetary Dynamos*, ed. M. R. E Proctor, P. C. Matthews & A. M. Rucklidge (Cambridge: Cambridge Univ. Press), p. 303
- Zweibel, E. G. & Heiles, C. 1997, *Nature*, 385, 131
- Zweibel, E. G., Heitsch, F. & Fan, Y. 2002, in *Simulations of Magnetohydrodynamic Turbulence in Astrophysics*, ed. T. Passot & E. Falgarone (Berlin: Springer), in press (astro-ph/0202525)

Table 1. Classification of turbulence/Time at the end of simulations, t_{end}

$\langle M_A \rangle_{\text{init}}$	10	20	50	100	200	300	1000	∞
512 ² ^a	FS ^b /80	FS ^b /100	<u>WF</u> ^b /40	VWF ^b /40	VWF ^b /40	VWF ^b /40	VWF ^b /40	HD ^b /40
1024 ² ^a	FS ^b /110	FS ^b /140	SF ^b /40	<u>WF</u> ^b /40	VWF ^b /40	VWF ^b /40	VWF ^b /40	HD ^b /40
1536 ² ^a			SF ^b /20	<u>WF</u> ^b /20	<u>WF</u> ^b /15	VWF ^b /20		HD ^b /20

^aThe number of grid cells used. The simulations with 256² grid cells were performed, but are not listed in tables.

^bStanding for field separation, strong field, weak field, very weak field, and hydrodynamic. See the text for details.

Table 2. Alfvén Mach number $\langle M_A \rangle$ /Mach number $\langle M_s \rangle$ for SF, WF, and VWF cases ^a

$\langle M_A \rangle_{\text{init}}$	50	100	200	300	1000	∞^b
512 ²	<u>2.38/0.83</u>	4.93/0.95	9.70/0.99	14.90/1.00	49.66/1.00	∞ /1.00
1024 ²	1.60/0.70	<u>3.02/0.86</u>	6.00/0.95	9.05/0.98	31.38/1.00	∞ /1.00
1536 ²	1.41/0.66	<u>2.28/0.81</u>	<u>4.04/0.85</u>	6.57/0.97		∞ /1.00

^aAveraged spatially over the whole computational domain, and temporally over $20 \leq t \leq t_{\text{end}}$ for 512² and 1024² simulations and over $10 \leq t \leq t_{\text{end}}$ for 1536² simulations. The values for the WF cases are underlined for clarity.

^bHydrodynamic turbulence.

Table 3. Density compression $\langle \delta\rho/\rho \rangle_{\text{rms}}$ /intermittency I for SF, WF, and VWF cases ^a

$\langle M_A \rangle_{\text{init}}$	50	100	200	300	1000	∞^b
512 ²	<u>0.32/2.68</u>	0.39/3.86	0.42/4.80	0.42/5.28	0.45/5.93	0.45/***
1024 ²	0.25/2.06	<u>0.34/3.03</u>	0.40/4.28	0.42/5.05	0.44/5.88	0.45/***
1536 ²	0.24/1.95	<u>0.30/2.48</u>	<u>0.37/3.48</u>	0.41/4.58		0.45/***

^aAveraged spatially over the whole computational domain, and temporally over $20 \leq t \leq t_{\text{end}}$ for 512² and 1024² simulations and over $10 \leq t \leq t_{\text{end}}$ for 1536² simulations. The values for the WF cases are underlined for clarity.

^bHydrodynamic turbulence.

Table 4. Spectral slope of kinetic energy/total energy for SF, WF, and VWF cases ^a

$\langle M_A \rangle_{\text{init}}$	50	100	200	300	1000	∞^b
512 ²	<u>2.22/1.27</u>	2.77/2.21	2.95/2.78	2.67/2.61	2.77/2.76	2.90/2.90
1024 ²	1.46/1.27	<u>2.07/1.20</u>	2.74/2.09	2.84/2.51	2.75/2.71	2.85/2.85
1536 ²	1.45/1.48	<u>1.68/1.18</u>	<u>2.33/1.50</u>	2.68/2.05		2.72/2.72

^aAveraged temporally over $20 \leq t \leq t_{\text{end}}$ for 512² and 1024² simulations and over $10 \leq t \leq t_{\text{end}}$ for 1536² simulations. Slops was fitted over the range of $2 \times k_{in} \leq k \leq k_{24}$. Here, k_{in} and k_{24} are the wavenumbers corresponding to the power input scale and 24 grid cells, respectively. The values for the WF cases are underlined for clarity.

^bHydrodynamic turbulence.

Fig. 1.— *Left panel* - Grey scale image of density for the non-magnetic case with 1536^2 resolution. Brighter regions correspond to higher values and the gray scale was set arbitrarily to highlight structures. The image represents the density distribution typical at an epoch ($t = 15$) after hydrodynamic turbulence is fully developed. *Right panel* - Power spectrum of kinetic energy, time-averaged over $10 \leq t \leq t_{\text{end}}$, for the non-magnetic case with 1536^2 resolution. Here, $k \equiv \sqrt{k_x^2 + k_y^2}$. The peak at $k = 5.7 \times 2\pi$ corresponds to the wavenumber of the power input scale, $k_{in} \equiv \sqrt{k_{in,x}^2 + k_{in,y}^2}$. For reference two vertical lines are drawn at $k = 2 \times k_{in}$ and the wavenumber corresponding to 8 grid cells, k_8 . Two lines with slopes of $-5/3$ and -3 are drawn for comparison.

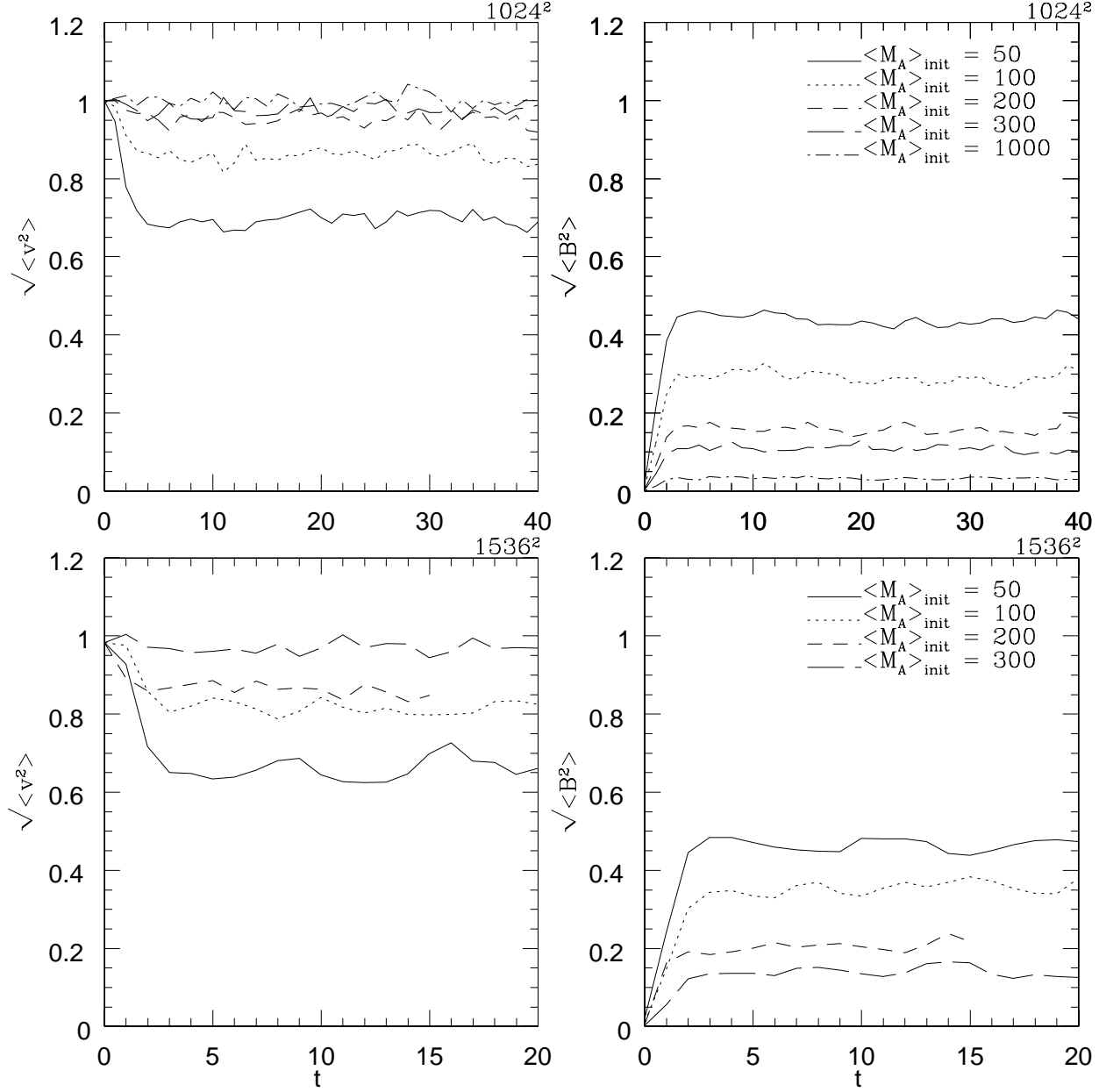


Fig. 2.— Time evolution of rms velocity (left panels) and magnetic field strength (right panels), which were averaged over one period of random forcing ($\tau = 1$), for different initial Alfvénic Mach numbers. Upper panels are for the cases with 1024^2 resolution and lower panels are for the cases with 1536^2 resolution.

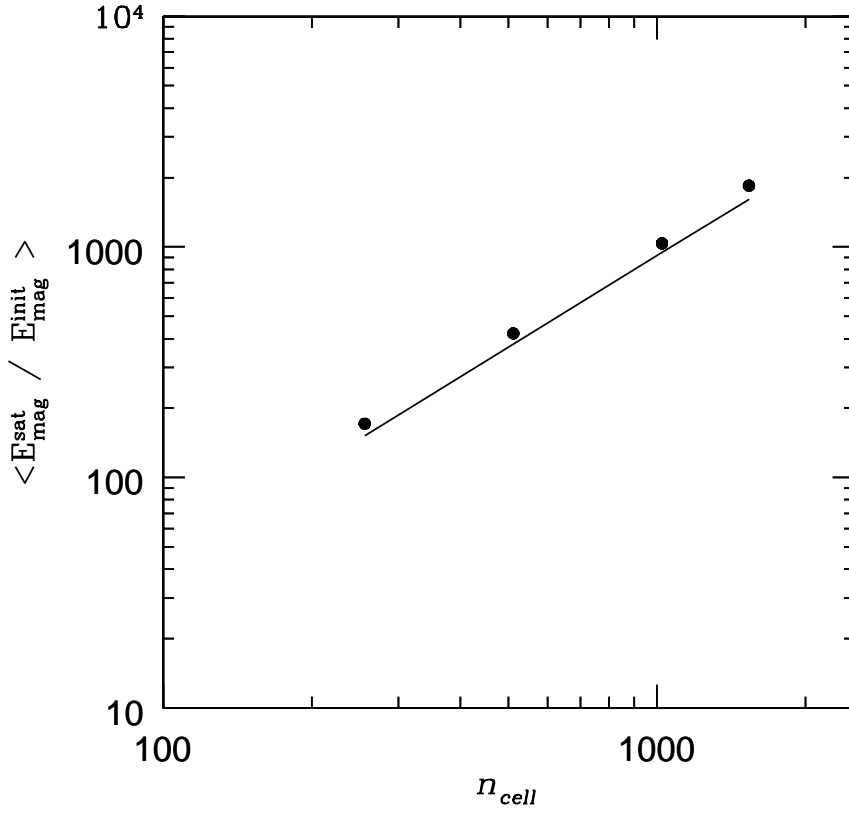


Fig. 3.— Averaged amplification of magnetic energy from the initial value in the VWF and WF cases as a function of numerical resolution. Four points of 256^2 , 512^2 , 1024^2 , and 1536^2 grid cells are plotted. The fitted line $\propto n_x^{1.32}$ is drawn.

Fig. 4.— Grey scale images of density (left panels) and contours of magnetic field lines (right panels) at an epoch ($t = 13$) for cases with 1536^2 resolution. Upper two panels are for the case of $\langle M_A \rangle_{\text{init}} = 50$ classified as the SF class, middle two panels are for $\langle M_A \rangle_{\text{init}} = 100$ classified as the WF class, and lower two panels are for $\langle M_A \rangle_{\text{init}} = 300$ classified as the VWF class. In the density images, brighter regions represent higher values and the gray scale was set arbitrarily to highlight structures.

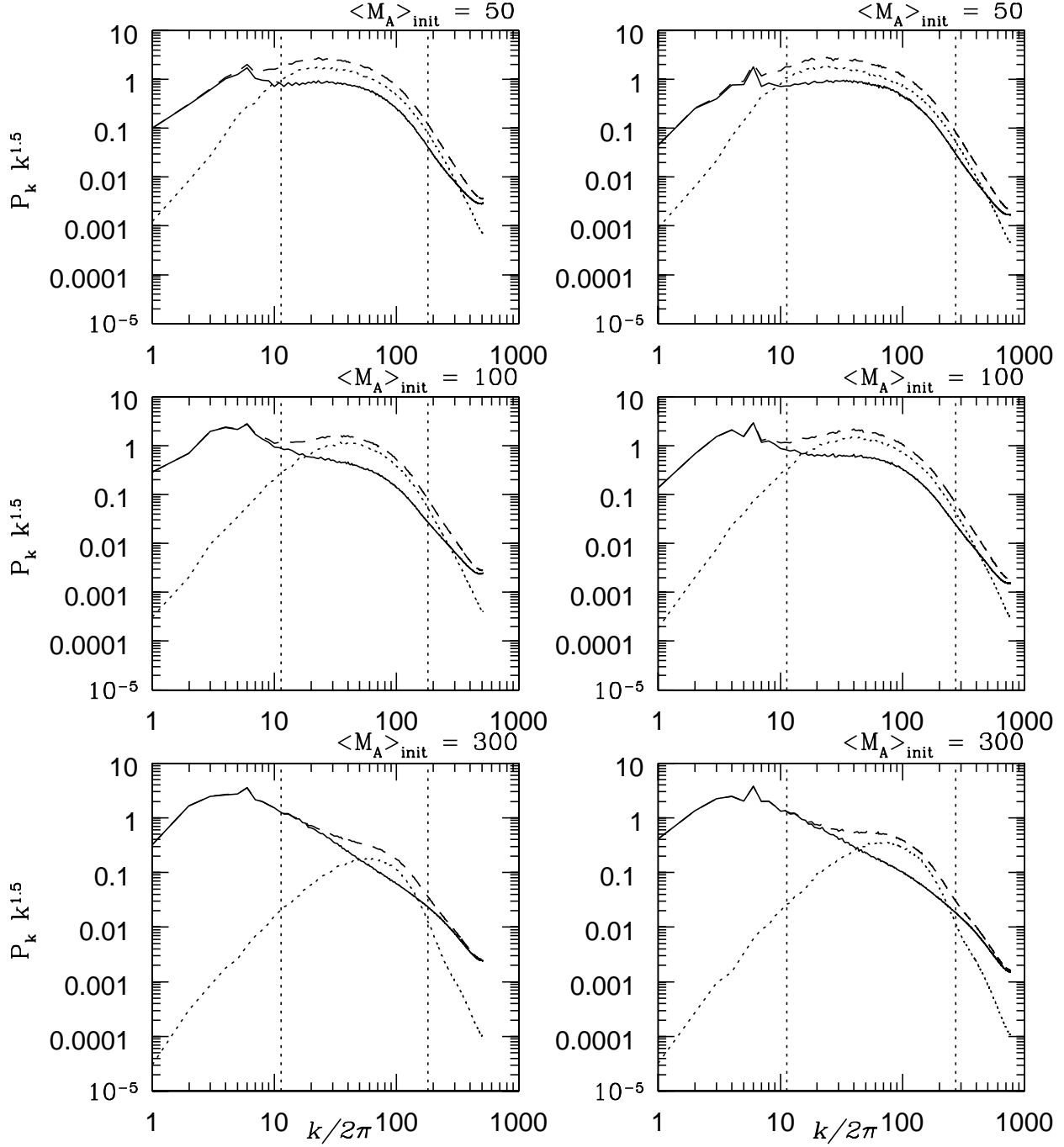


Fig. 5.— Power spectra, time-averaged over $20 \leq t \leq t_{\text{end}}$ for 1024^2 resolution (left panels) and over $10 \leq t \leq t_{\text{end}}$ for 1536^2 resolution (right panel). Spectra are multiplied by $k^{1.5}$ for clarity. Solid line - power spectrum of kinetic energy, P_k^{kin} , dotted line - power spectrum of magnetic energy, P_k^{mag} , and dashed line - power spectrum of total energy, P_k^{tot} . From top to bottom correspond to the SF, WF, and VWF classes, respectively. The slopes fitted over the range of $2 \times k_{\text{in}} \leq k \leq k_{24}$ are shown in Table 4. Here k_{24} is the wavenumbers corresponding to 24 grid cells.

Fig. 6.— Contours of magnetic field lines at four different times for the case of $\langle M_A \rangle_{\text{init}} = 10$ with 1024^2 resolution. It belongs the FS class.

This figure "f1.jpg" is available in "jpg" format from:

<http://arxiv.org/ps/astro-ph/0305165v1>

This figure "f4.jpg" is available in "jpg" format from:

<http://arxiv.org/ps/astro-ph/0305165v1>

This figure "f6.jpg" is available in "jpg" format from:

<http://arxiv.org/ps/astro-ph/0305165v1>